Supporting Information.

Giant Current-Perpendicular-to-Plane Magnetoresistance in Multilayer Graphene as Grown on Nickel

S. C. Bodepudi, A. P. Singh and S. Pramanik*

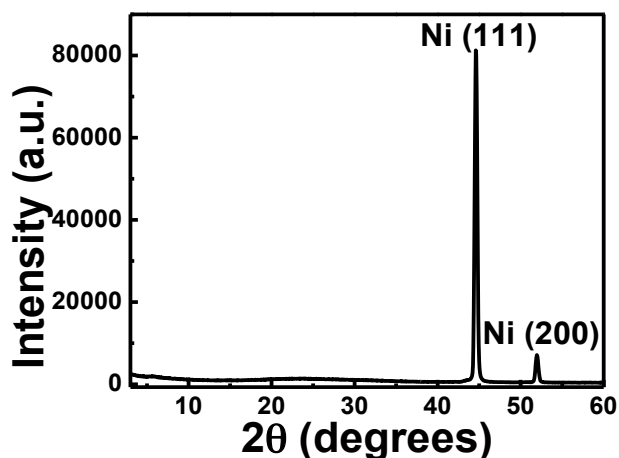Department of Electrical and Computer Engineering, University of Alberta, Edmonton, Alberta T6G 2V4, Canada

* **Email:** spramani@ualberta.ca

Experimental Details.

I. Growth of Multilayer Graphene (MLG) on Ni Substrates Using Chemical Vapor Deposition (CVD).

Multilayer graphene (MLG) has been grown on polycrystalline nickel (Ni) substrates (25μm thick, annealed, 99.5% metal basis, purchased from Alfa Aesar) in a commercial Tystar chamber using a standard chemical vapor deposition (CVD) method[1–4]. **Figure S1** shows the X-ray diffraction (XRD) spectrum of the Ni foil, indicating the presence of predominantly Ni (111) grains with a small population of Ni (100) grains. Similar polycrystalline Ni substrates have been used by various groups in the past for graphene growth[1,4].

CVD process flow consists of the following steps: (a) Ni substrate (~ 2 cm × 2 cm in size) load, (b) furnace purge, (c) temperature ramp to 1000°C and hydrogen anneal for one hour, (d) graphene growth at 1000°C for 10 minutes, (e) natural cooling, and finally (f) unloading of the sample. We have used 0.3% CH_4, 9.7% H_2, and 90% Ar during the growth of graphene. This growth process results in absence of D peak and absence of significant splitting in the $2D$ peak in the Raman spectra (Figure 1b, main text). These features are correlated with the observation of large negative CPP-MR (Figure 2, main text). Higher relative concentration of carbon-containing species within the chamber leads to bulk graphite (HOPG-like) growth on the Ni surface[3,5], which exhibits HOPG-like Raman $2D$ band (Figure 4a, main text). The hydrogen anneal step removes the native oxide layer and any adsorbate from the Ni surface.

Figure S1: XRD spectrum of the Ni substrate used for CVD growth of MLG.

II. Transfer of MLG on SiO$_2$/Si Substrate and Raman Characterization.

In the main text, we have shown Raman spectra from representative regions of the as-grown MLG on Ni (Figure 1b, top inset). The MLG has also been characterized after transferring on SiO$_2$/Si substrates. Transfer of MLG has been performed as follows[2,3]. We first spin coated PMMA on the top graphene surface. Since graphene growth takes place on both surfaces of the Ni foil, we removed the back graphene layer using plasma etching and exposed the Ni substrate. (Similar steps have been followed while preparing samples for magnetotransport measurements, where the Ni substrate acts as an electrical contact). The Ni substrate was then etched away using warm ($\sim 60^o$C) ferric chloride (FeCl$_3$) solution. The etching process takes $\sim 4-5$ hours to complete. Upon completion of the etching step, MLG/PMMA composite film floats up in the FeCl$_3$ solution. MLG/PMMA film was collected and thoroughly cleaned in deionized water. Next, the cleaned MLG/PMMA film was transferred on a SiO$_2$ (300nm)/Si wafer. After overnight drying we heated the sample ($\sim 250^o$ C) in a vacuum oven so that the graphene layer adheres strongly to SiO$_2$ surface. Finally, top PMMA layer was dissolved in acetone, which left only MLG layer on SiO$_2$ surface.

Figure S2 (a) shows typical Raman characteristics of transferred MLG. All Raman spectra in this work have been acquired at room temperature using a Nicolet Almega XR Micro and Macro Raman Analysis System. Laser wavelength is set to 532nm (2.33eV). Maximum power is set to 24mW, 100% of which has been used for all studies. No evidence of laser induced heating[6] has been found in any case. Unlike as-grown MLG, the *2D* band in the Raman spectrum resembles HOPG-like *2D* band with a shoulder in the lower frequency range of the band. Such change in Raman characteristics has been observed before by other groups[1,3,7]and can be attributed to the above-mentioned thermal processing steps involved in the transfer process.

Annealing or heat treatment indeed causes "graphitization" of turbostratic graphite. For example, ref.[7] started out with a turbostratic graphite sample in which the *2D* peak is symmetric and does not show any splitting. For this sample as discussed in the main text, interaction between the basal planes is weak enough so that the splitting in the π electrons' dispersion energies does not occur resulting in a single Lorentzian in the *2D* band. However after heat treatment, the *2D* band resembles the shoulder-like shape of HOPG, indicating splitting of the π electrons' dispersion

energies. Such splitting indicates presence of significant interlayer coupling as compared to the starting turbostratic sample. Presumably, the heat treatment gives rise to planar rearrangement of the carbon atoms, which stabilizes to stronger interlayer coupling (Bernal stacked) configuration after the sample is cooled. Our observation is consistent with this work because during the transfer process we have used high temperature (250°C) vacuum annealing to achieve substrate adhesion and reliable electrical measurements.

On a related note, ref.[8] observed change in the *2D* band of monolayer graphene as a function of annealing temperature. In this case, however, interlayer coupling is irrelevant since the sample consists of only one layer of graphene. In this work the change in the *2D* band has been explained by invoking the compressive stress induced by the SiO_2 substrate.

We did try to carry out (CPP) electrical measurements after transfer and without annealing. Unfortunately, without annealing, the electrical contact (and adhesion) between bottom electrode and transferred MLG was poor and we were unable to get reliable electrical measurements. The transferred MLG films tend to peel off the substrate in absence of annealing. Such poor contact and poor adhesion to the bottom substrate presumably results from water or air molecules trapped in a "dead space" between MLG and the bottom contact. Annealing helps to compress this "dead space" via desorption of such species and significantly improves the quality of the bottom electrical contact (after transfer) but unfortunately destroys the weak interlayer coupling. Improvement of surface adhesion upon annealing has also been observed by other groups[9,10].
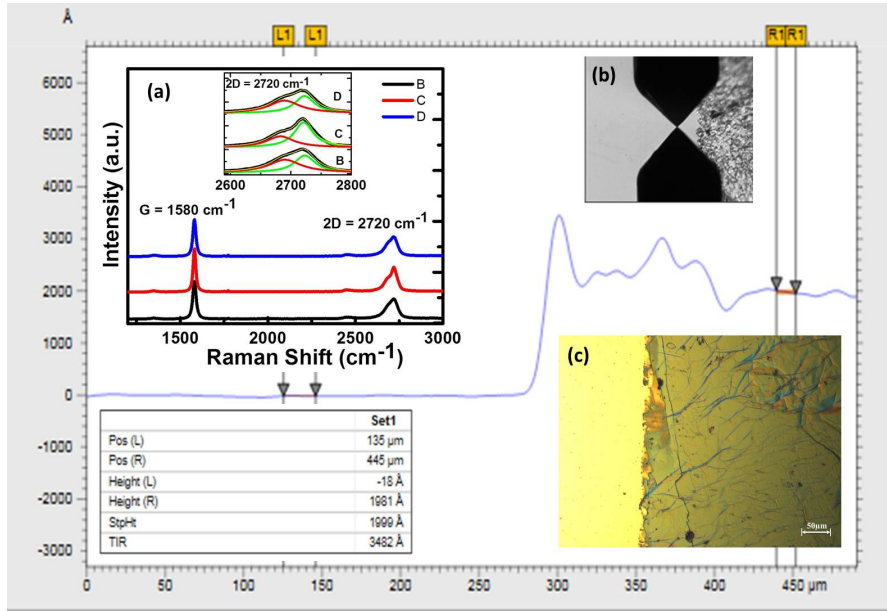
There are other advantages of post-transfer annealing as well. For example, annealing is often used to desorb and decompose the chemical (primarily PMMA) residues that remain on graphene as a result of the transfer process[9–11]. Such residues cause unintentional doping of the graphene layers and results in a shift of the Fermi level from the Dirac point. Since the CPP-MR is due to interlayer tunneling between the zero mode Landau levels that are located at the Fermi levels, such shift in the Fermi levels is undesirable. Annealing is necessary to avoid this effect.

We also note that the Ni etching step involves using hot (~ 60°C) $FeCl_3$ solution for ~ 4-5 hours. Using cold/room temperature solutions does not etch Ni completely even after prolonged etching

and leaves significant amount of Ni residues. Use of hot solutions for long time during etching can also adversely affect the weak interlayer coupling.

Thus such elevated temperature processes are necessary for proper transfer and electrical measurements of MLG and these processes adversely affect the interlayer coupling. Therefore as discussed in the main text we employed alternative control experiments in which such transfer steps are avoided (Figures 3c, d, 4).

Figure S2 (b), (c) show optical microscopic images of the transferred MLG, which indicate presence of multiple layers of graphene. In **Figure S2 (main image)** we show the step height measurement, which indicates average thickness of MLG is ~ 200 nm. Wrinkles in the graphene layer are clearly visible, which is a characteristic of CVD-grown graphene[5].

Figure S2. Characterization of the MLG samples transferred on SiO$_2$/Si. (*a*) Raman spectra, indicating HOPG-like distorted *2D* band. (*b*), (*c*) Optical images of the transferred MLG. The main image shows the step height measurement.

Transport measurements on such transferred samples have been reported in sections III and IX of this document.

III. In-plane MR of Transferred MLG and Estimation of Ag paste/MLG Contact Resistance.

Devices for in-plane measurements have been fabricated in two different ways. In one method, MLG has been transferred on Au fingers patterned on SiO_2 substrate. Au wires have been attached to these fingers by using Ag paste. Thus in these devices the MLG is actually contacted by Au fingers and not directly by Ag paste. Transfer process of the MLG has been described previously in section II of this document. In the second method electrical contacts are directly made on the top surface of transferred MLG by Ag paste.
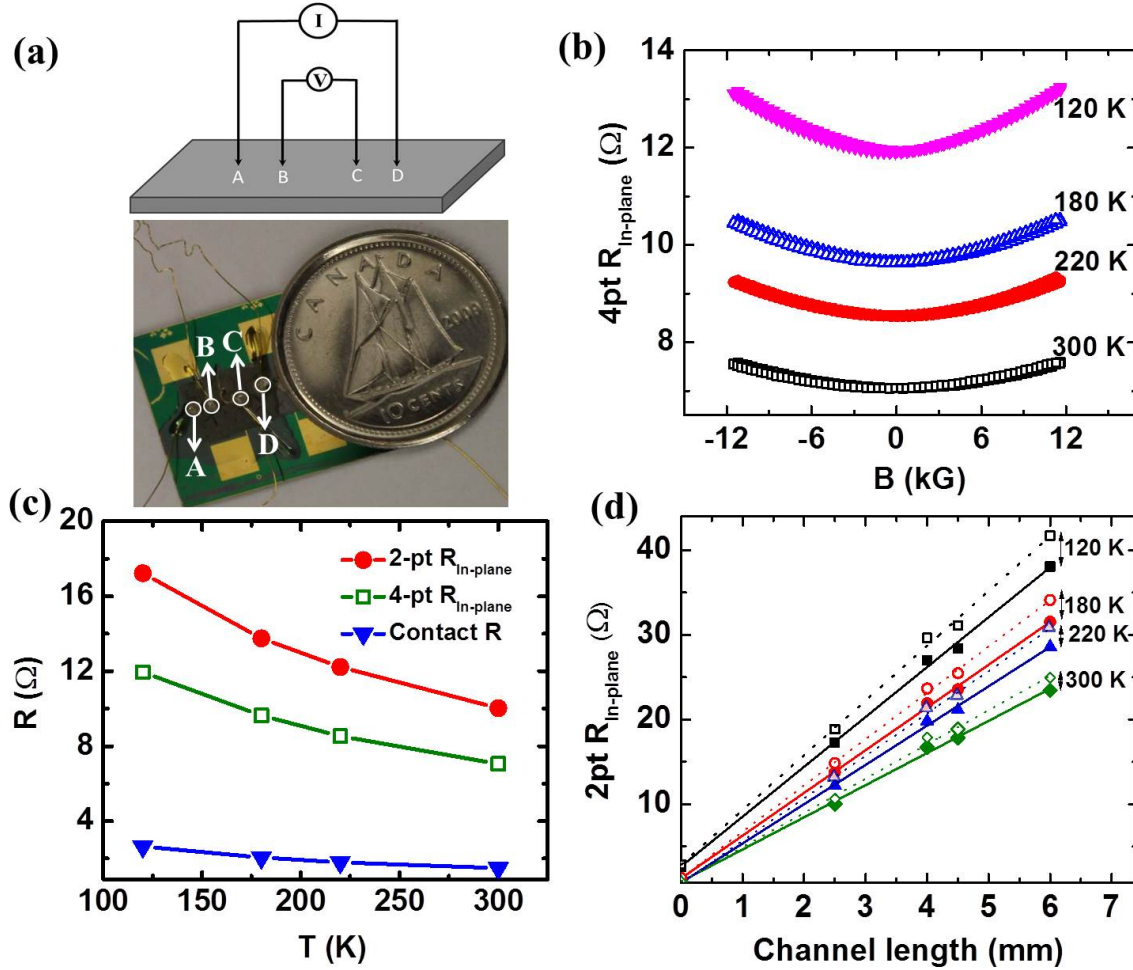
A digital image of the in-plane device and measurement geometry are shown in **Figure S3 (a)**. Distance between neighboring electrical contacts is ~ 1mm. Contact area is ~ $1mm^2$ (same as in our CPP devices). Similar in-plane device dimensions have been reported in some recent work such as ref.s [12–14].

In-plane resistance has been measured by both two-probe and four-probe methods. Devices contacted by Au fingers or Ag paste show nominally identical (in-plane) MR behavior. Since devices in which Ag paste contacts have been made directly on graphene are directly relevant for our study (since they allow estimation of Ag paste/graphene contact resistance), we present data from these devices in **Figure S3 (b)**.

Figure S3 (b) shows in-plane MR (measured in a four probe geometry, Ag-paste contacts directly made on MLG) of the transferred MLG sample. In-plane resistance exhibits insulating temperature dependence, which is consistent with ref.[15]. MR data has been taken in presence of an out-of-plane magnetic field. No strong negative MR signal has been observed. We only observe weak positive MR (~ 8% at 120K and ~ 7% at 300K). Thus the MR response reported in Figure 2 (main paper) must originate from out-of-plane carrier transport.

We have evaluated the (zero magnetic field) contact resistance between Ag paste and MLG using two different methods. First, the two-point and four-point resistances have been measured (**Figure S3 (c)**) between the inner pair of contacts (B and C) in Figure S3 (a). Contact resistance has been estimated as [two-point-resistance – four-point-resistance]/2. Two-point and four-point data have been collected by Picotest M3500 multimeter as well as Keithley 2636 Dual Channel

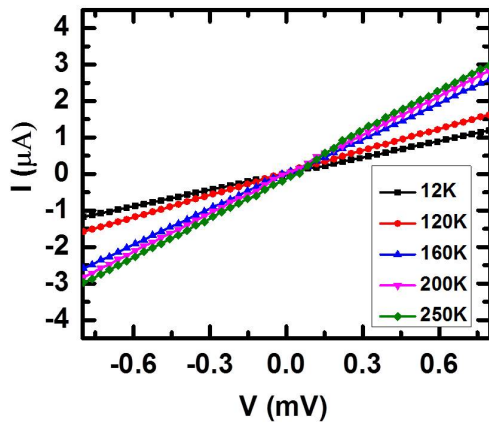Source Meter. Excellent agreement has been obtained between the readings of these two equipments.

Figure S3. In-plane Measurements. (a) Four point measurement geometry and digital image of the device. Ag paste contacts have been made directly on MLG (contact area ~ 1mm^2). Distance between neighboring contacts is ~ 1mm. Au pads have not been used in this study and they generally produce results nominally identical to those presented here. (b) In-plane four-point MR of transferred (Ni-grown) MLG. (c) Two-point and four-point in-plane resistance at zero magnetic field. Contact resistance has been estimated as half of the difference between two-point and four-point data. (d) In-plane two-point resistance vs. channel length (i.e. distance between the two contacts). Closed symbols and solid line fits correspond to zero magnetic field case whereas open symbols and dashed line fits correspond to the case when 11kG out-of-plane magnetic field is present. The linear trends extrapolated to zero channel length limit provide an estimate of the Ag paste/MLG contact resistance.

Next, we have plotted two-point resistance (zero magnetic field) as a function of the distance between contacts (or "channel length") in **Figure S3 (d)**. Two-point resistance has been found to increase linearly with increasing channel length. This linear trend, extrapolated to zero channel length limit, should give us an estimate of the contact resistance since contact resistance is independent of channel length. In Figure S3 (d) solid lines and filled symbols correspond to zero magnetic field measurements. Same current bias (1mA) has been used in all measurements (in-plane two-point and four-point in Figure S3, out-of-plane in Figures 2 and 3(a)).

Contact resistances estimated by these two methods match closely and in all cases contact resistance is $\sim 1 - 3$ Ohms. This value is two orders of magnitude smaller than the (zero field) CPP resistance reported in Figure 2. Further, the contact resistance does not depend significantly on magnetic field. In Figure S3 (d) we also show the two-point-resistance vs. channel length data taken at 11kG (open symbols, dashed lines). As expected in presence of magnetic field resistance values are slightly higher compared to the corresponding zero magnetic field values (positive in-plane MR effect). However they depend linearly on channel length and the extrapolated values in the limit of zero channel length match very well with the zero field case. Thus, Ag paste/graphene contact resistance does not play any crucial role in our reported CPP MR data.

IV. I-V Characteristics (CPP Geometry) at Zero Magnetic Field.

Figure S4 below shows the zoomed-in zero-field *I-V* characteristics. No non-linearity has been observed and these characteristics are very similar to the high-field *I-V* data. Thus magnetic field induced switching of current path can be ruled out as a possible cause of the observed MR effect.
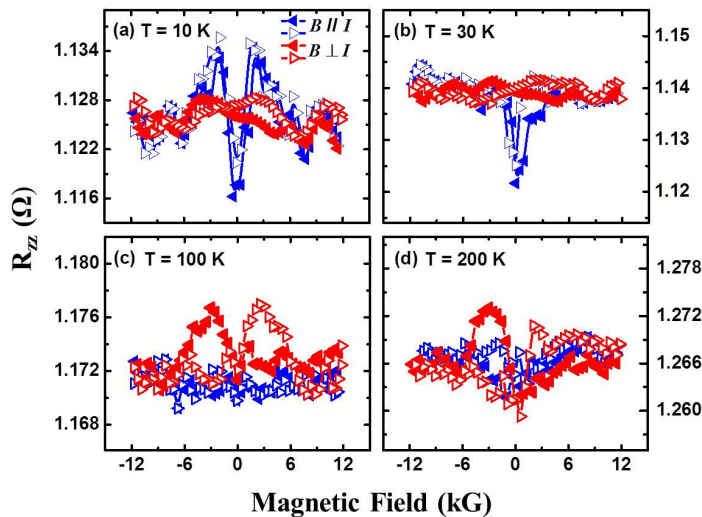

Figure S4. Magnified plot of the zero-field *I-V* characteristics shown in Figure 3b (main text).

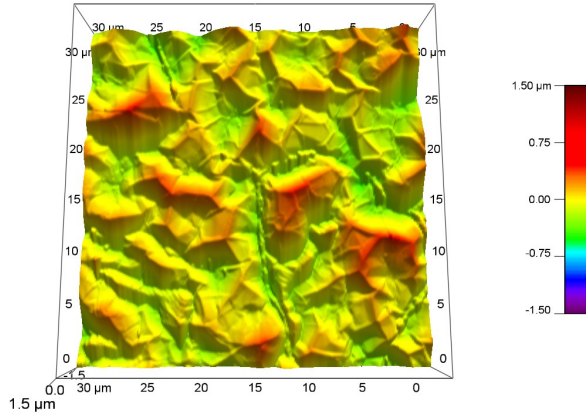## V. Magnetoresistance (MR) Measurements on Ni Substrates.

For all magnetoresistance (MR) measurements, Model 642 electromagnet power supply and Cryotronics 332 Controller (Lakeshore) have been used as electromagnet current source and temperature controller respectively. Picotest M3500 multimeter has been used to directly extract the resistance of the device. Each resistance value is the average of 50 readings. The measured resistance values have been independently validated by a Keithley Model 2636 dual-channel system source meter. A 475 DSP gauss meter has been used to record the magnetic field values. All equipments have been synchronized by LabView VI for data acquisition.

Anisotropic magnetoresistance (AMR) of the bottom Ni contact has no effect on the observed MR data due to the following reasons: (a) the typical AMR effect is ~1% (**Figure S5**), whereas we have observed ~10^4% MR in Figure 2, (b) the CPP resistance of the Ni substrate is ~100 times smaller than the CPP resistance of MLG/Ni composite and hence any MR of Ni substrate will be negligible in the MR of MLG/Ni composite and (c) CPP resistance of the composite exhibits a semiconducting temperature-dependence (Figure 3a, main text) and not a metallic temperature-dependence as shown below. Thus we can rule out possibility of any artifact due to AMR of Ni. Based on above considerations we can also rule out the possibility of any pinhole short between top Ag contact and bottom Ni substrate.

Figure S5. Typical AMR response of Ni foil substrate. The symbols indicate scan directions.
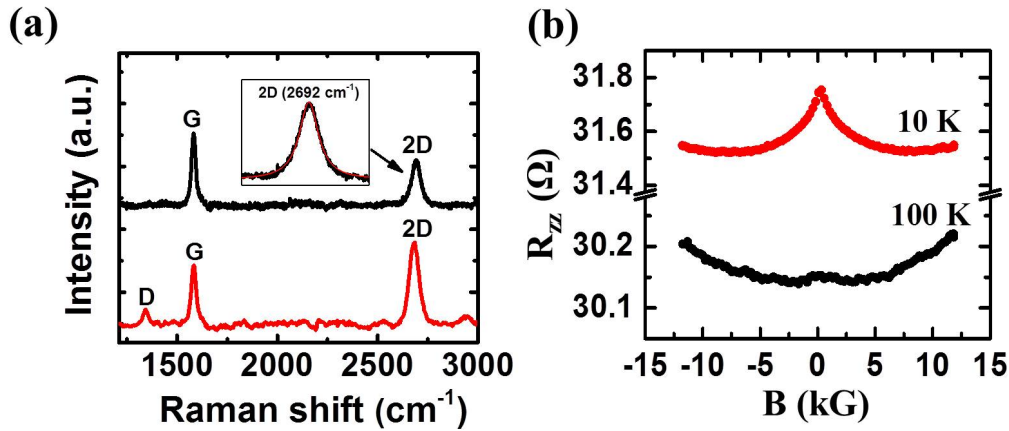
VI. AFM Image of Multilayer Graphene Grown on Ni Foil.

Figure S6. Atomic Force Microscopic (AFM) image of CVD-grown MLG-on-Ni.

We used AFM (Asylum Research, MFP-3D) under ambient conditions with a standard tetrahedral silicon tip (Olympus, OMCLAC160TS-W2) located at the end of a silicon cantilever to get surface roughness profile of CVD-grown MLG-on-Ni. Under AC mode, the typical values of force constant, resonant frequency and scan rate were 42 N/m, 300 kHz and 1 Hz respectively. The radius of curvature of the tip is < 10nm.
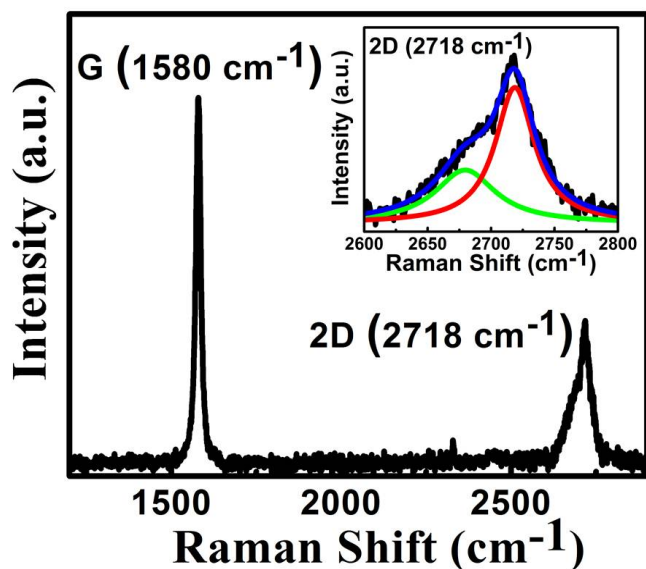
VII. CPP MR of MLG CVD-Grown on Cu.

Figure S7. (*a*) Raman characteristics of MLG (~ 8 layer) CVD-grown on copper (ACS Materials). The bottom scan is taken from the grain boundary region, which shows a significant defect (*D*) peak. (*b*) CPP-MR of MLG/copper, showing weak localization at low field, which disappears at higher temperature. This is consistent with ref.[16], which studied MLG on Cu, prepared by a layer-by-layer transfer process.

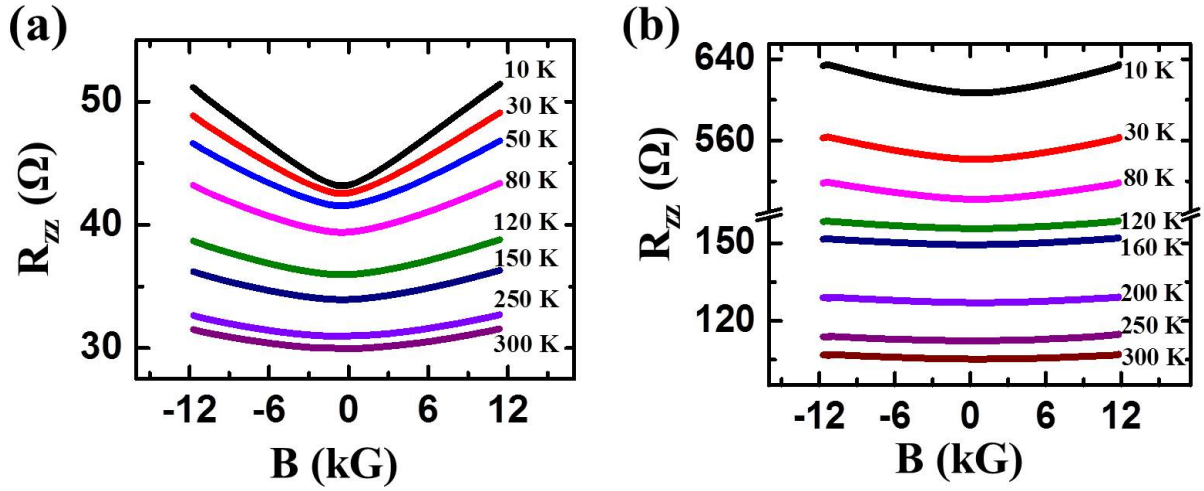## VIII. Raman Characterization of Highly Oriented Pyrolytic Graphite (HOPG).

Figure S8 below shows Raman spectrum of *HOPG graphite* (SPI supplies, SPI-1 grade, 10 x 10 x 1 mm). The two characteristic peaks of HOPG occur at ~ 1580 cm^{-1} and ~ 2718 cm^{-1} (Figure S8) which are commonly labeled as *G* and *2D* peak respectively[17,18]. The *2D* peak for HOPG is asymmetric (inset of Figure S8), consists of two shifted Lorentzian components and the higher intensity component appears at higher frequency side.
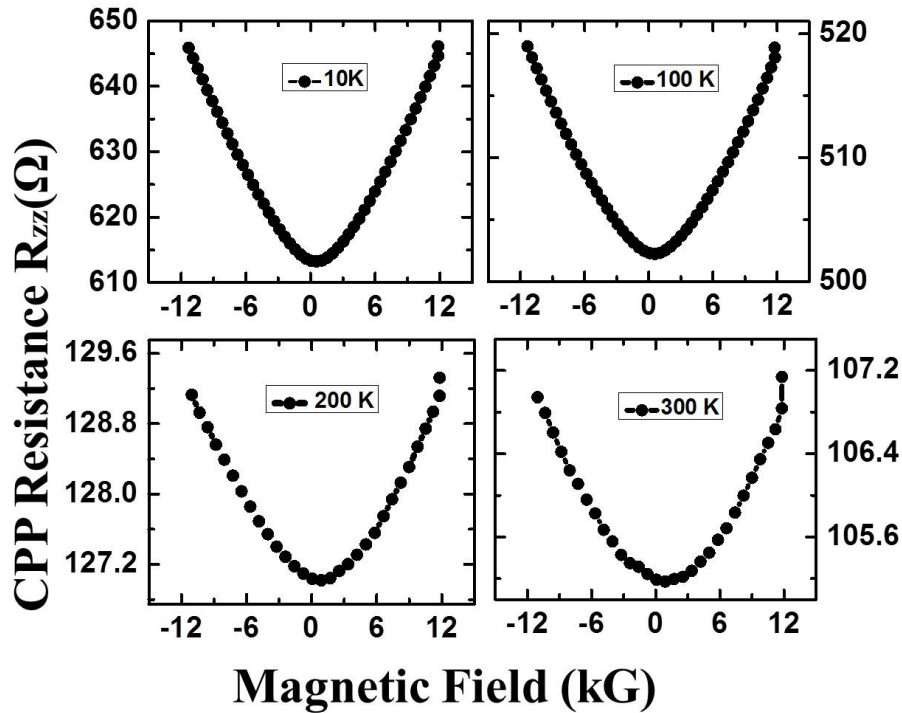

Figure S8: (*main image*) Raman spectrum of HOPG from SPI supplies. (*inset*) Magnified *2D* peak and the Lorentzian fits.

IX. CPP MR of MLG Transferred on Au and Ni Electrodes.

As mentioned in the main text, the MLG samples transferred on Au and Ni electrodes do not exhibit any large negative CPP-MR, but show a weak positive CPP-MR instead. The CPP-MR responses of these transferred samples are shown below (**Figures S9, S10**). As noted before, unlike as-grown samples, the transferred MLG exhibits a shoulder in the 2*D* Raman band (Figure S2).
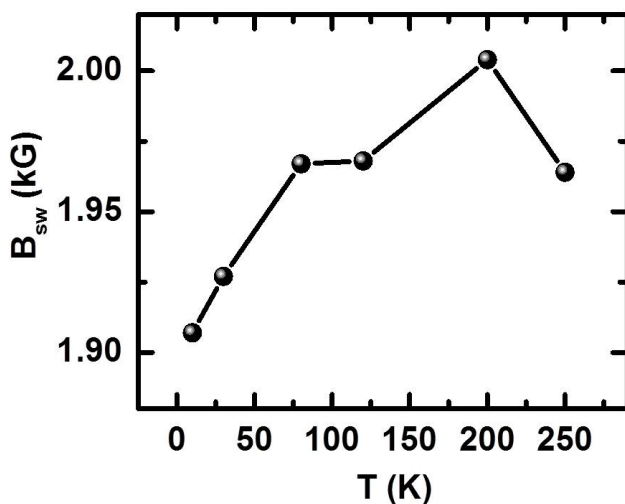
(a)

(b)

Figure S9. (*a*) CPP-MR of MLG (Ni-grown) transferred on Au contact and (*b*) CPP-MR of MLG (Ni-grown) transferred on Ni contact (Magnified image is shown in Figure S10 below). No weak-localization related negative MR has been observed due to presence of larger number of graphene layers. This is also consistent with ref.[16]. The transferred MLG exhibits shoulder peak in Raman 2*D* band (Figure S2).

Figure S10. Positive CPP MR (magnified) of MLG transferred on Ni electrodes.

X. Switching Magnetic Field as a Function of Temperature.

It is clear from Figure 2 (main text) that the sharp drop in CPP resistance takes place near a "switching magnetic field (B_{SW})". **Figure S11** below shows the temperature dependence of the switching field. In this plot B_{SW} is taken to be the field value at which resistance decreases to 50% of its zero-field value. A weak increasing trend has been observed which is consistent with the interlayer tunneling model since at higher temperature higher magnetic field will be needed to overcome thermal broadening.

Figure S11. Switching magnetic field as a function of temperature.

References

(1) Yu, Q.; Lian, J.; Siriponglert, S.; Li, H.; Chen, Y. P.; Pei, S.-S. *Applied Physics Letters* **2008**, *93*, 113103–113103–3.
(2) Reina, A.; Jia, X.; Ho, J.; Nezich, D.; Son, H.; Bulovic, V.; Dresselhaus, M. S.; Kong, J. *Nano Lett.* **2008**, *9*, 30–35.
(3) Kim, K. S.; Zhao, Y.; Jang, H.; Lee, S. Y.; Kim, J. M.; Kim, K. S.; Ahn, J.-H.; Kim, P.; Choi, J.-Y.; Hong, B. H. *Nature* **2009**, *457*, 706–710.
(4) Zhang, Y.; Gomez, L.; Ishikawa, F. N.; Madaria, A.; Ryu, K.; Wang, C.; Badmaev, A.; Zhou, C. *J. Phys. Chem. Lett.* **2010**, *1*, 3101–3107.
(5) Chae, S. J.; Güneş, F.; Kim, K. K.; Kim, E. S.; Han, G. H.; Kim, S. M.; Shin, H.-J.; Yoon, S.-M.; Choi, J.-Y.; Park, M. H.; Yang, C. W.; Pribat, D.; Lee, Y. H. *Advanced Materials* **2009**, *21*, 2328–2333.
(6) Everall, N. .; Lumsdon, J.; Christopher, D. . *Carbon* **1991**, *29*, 133–137.

(7) Cançado, L. G.; Takai, K.; Enoki, T.; Endo, M.; Kim, Y. A.; Mizusaki, H.; Speziali, N. L.; Jorio, A.; Pimenta, M. A. *Carbon* **2008**, *46*, 272–275.

(8) Ni, Z. hua; Wang, Y. ying; Yu, T.; Shen, Z. xiang. *arXiv:0810.2836* **2008**.

(9) Pirkle, A.; Chan, J.; Venugopal, A.; Hinojos, D.; Magnuson, C. W.; McDonnell, S.; Colombo, L.; Vogel, E. M.; Ruoff, R. S.; Wallace, R. M. *Applied Physics Letters* **2011**, *99*, 122108.

(10) Cheng, Z.; Zhou, Q.; Wang, C.; Li, Q.; Wang, C.; Fang, Y. *Nano Lett.* **2011**, *11*, 767–771.

(11) Lin, Y.-C.; Lu, C.-C.; Yeh, C.-H.; Jin, C.; Suenaga, K.; Chiu, P.-W. *Nano Lett.* **2012**, *12*, 414–419.

(12) Wang, Y. Y.; Burke, P. J. *Applied Physics Letters* **2013**, *103*, 052103.

(13) Yang, G.; Lee, C.; Kim, J.; Ren, F.; Pearton, S. J. *Phys. Chem. Chem. Phys.* **2013**, *15*, 1798–1801.

(14) Shen, T.; Wu, W.; Yu, Q.; Richter, C. A.; Elmquist, R.; Newell, D.; Chen, Y. P. *Applied Physics Letters* **2011**, *99*, 232110.

(15) Heo, J.; Chung, H. J.; Lee, S.-H.; Yang, H.; Seo, D. H.; Shin, J. K.; Chung, U.-I.; Seo, S.; Hwang, E. H.; Das Sarma, S. *Phys. Rev. B* **2011**, *84*, 035421.

(16) Liao, Z.-M.; Wu, H.-C.; Kumar, S.; Duesberg, G. S.; Zhou, Y.-B.; Cross, G. L. W.; Shvets, I. V.; Yu, D.-P. *Advanced Materials* **2012**, *24*, 1862–1866.

(17) Malard, L. M.; Pimenta, M. A.; Dresselhaus, G.; Dresselhaus, M. S. *Physics Reports* **2009**, *473*, 51–87.

(18) Charlier, J.; Eklund, P.; Zhu, J.; Ferrari, A. In *Carbon Nanotubes*; Springer Berlin / Heidelberg, 2008; Vol. 111, pp. 673–709.